Supporting Information

Immersion Condensation on Oil-infused Heterogeneous Surfaces for Enhanced Heat Transfer

Rong Xiao[1], Nenad Miljkovic[1], Ryan Enright[1,2,§], and Evelyn N. Wang[1*]

[1]Department of Mechanical Engineering, Massachusetts Institute of Technology, Cambridge, Massachusetts, USA
[2]Stokes Institute, University of Limerick, Limerick, Ireland
[§]Current address: Thermal Management Research Group, Efficient Energy Transfer (ηET) Dept., Bell Labs Ireland, Alcatel-Lucent Ireland Ltd., Blanchardstown Business & Technology Park, Snugborough Rd, Dublin 15, Ireland

*Address correspondence to: enwang@mit.edu

S1. Parameters affecting the condensation heat transfer coefficient

Based on the model developed by Miljkovic *et al.*,[1] on a dropwise condensation surface, the heat transfer rate through a single growing droplet can be determined as

$$q = \frac{\Delta T}{R_{tot}} = \frac{\pi R^2 \left(\Delta T - \frac{2T_{sat}\sigma}{Rh_{fg}\rho_w}\right)}{\frac{1}{2h_i(1-cos\theta)}} + \frac{R\theta}{4k_w sin\theta} + \frac{1}{k_{HC}\sin^2\theta}\left[\frac{k_P\phi}{\delta_{HC}k_P + hk_{HC}} + \frac{k_w(1-\phi)}{\delta_{HC}k_w + hk_{HC}}\right]^{-1} \quad \text{(E1)}$$

where R_{tot} is the total thermal resistance through the droplet, R is the droplet radius, ρ_w is the liquid water density, h_{fg} is the latent heat of vaporization, T_{sat} is the vapor saturation temperature, σ is the water surface tension, ΔT is the temperature difference between the saturated vapor and substrate ($T_{sat} - T_s$), δ_{HC} and h are the hydrophobic coating thickness (~ 1 nm) and pillar height, respectively, k_{HC}, k_w, and k_P are the hydrophobic coating, water, and pillar thermal conductivities, respectively, and h_i is the interfacial condensation heat transfer coefficient.[2] ϕ is the solid fraction of the micro/nanostructures. In the special case of a flat surface, we have $\phi = 1$ and $h = 0$.

Droplet size distribution theory was considered to determine the fraction of droplets with a given radius, *R*, in the droplet heat transfer model. For small droplets, the droplet distribution is determined by[3]

$$n(R) = \frac{1}{3\pi {R_e}^3 \hat{R}} \left(\frac{R_e}{\hat{R}}\right)^{-2/3} \frac{R(R_e - R^*)}{R - R^*} \frac{A_2 R + A_3}{A_2 R_e + A_3} \exp(B_1 + B_2) \tag{E2}$$

where

$$B_1 = \frac{A_2}{\tau A_1}\left[\frac{{R_e}^2 - R^2}{2} + R^*(R_e - R) - {R^*}^2 ln\left(\frac{R - R^*}{R_e - R^*}\right)\right] \tag{E3}$$

$$B_2 = \frac{A_3}{\tau A_1}\left[R_e - R - R^* ln\left(\frac{R - R^*}{R_e - R^*}\right)\right] \tag{E4}$$

$$\tau = \frac{3{R_e}^2\left({A_2}^2 R_e + A_3\right)^2}{A_1\left(11A_2{R_e}^2 - 14A_2 R_e R^* + 8A_3 R_e - 11A_3 R^*\right)} \tag{E5}$$

$$A_1 = \frac{\Delta T}{h_{fg}\rho_w(1 - cos\theta)^2(2 + cos\theta)} \tag{E6}$$

$$A_2 = \frac{\theta}{4k_w sin\theta} \tag{E7}$$

$$A_3 = \frac{1}{2h_i(1 - cos\theta)} + \frac{1}{k_{HC} sin^2\theta}\left[\frac{k_P \phi}{\delta_{HC} k_P + h k_{HC}} + \frac{k_w(1 - \phi)}{\delta_{HC} k_P + h k_{HC}}\right]^{-1} \tag{E8}$$

$\hat{R}$ is the average departure radius, R^* is the critical droplet size for nucleation, τ is the droplet sweeping period, and R_e is the radius when droplets begin to merge and grow by droplet coalescence afterwards, $R_e = l_C/2$ with l_c being the coalescence length determined by nucleation density, *N*

$$l_C = (4N)^{-2} \tag{E9}$$

For large droplets growing mainly due to coalescence, the droplet distribution can be determined as[4]

$$N(R) = \frac{1}{3\pi R^2 \hat{R}} \left(\frac{R}{\hat{R}}\right)^{-2/3} \tag{E10}$$

The total surface condensation heat flux, *q''*, can be obtained by incorporating the individual droplet heat transfer rate (Eqn. E1) with the droplet size distributions (Eqns. E2 and E10)

$$q" = \int_{R^*}^{R_e} q(R)n(R)dR + \int_{R_e}^{\hat{R}} q(R)N(R)dR \tag{E11}$$

The total condensation heat transfer coefficient is determined as

$$h_C = q"/\Delta T \tag{E12}$$

Therefore, the sensitivity of h_c on the departure radius, advancing contact angle and nucleation density can be obtained as shown in Fig. 1 in the manuscript.

S2. Estimation of local contact angle on high-surface-energy sites with the existence of oil

As shown in Fig. F1(a), on a high-surface-energy domain of the TFTS coating without oil-infusion, the local contact angle of a water droplet on a surface, $\theta_{ws(v)}$, can be determined using Young's equation as

$$cos\theta_{ws(v)} = \frac{\sigma_{vs} - \sigma_{ws}}{\sigma_{wv}} \tag{E13}$$

where σ_{vs} is the interfacial energy between the surface and vapor, σ_{ws} is the interfacial energy between water and the surface, and σ_{wv} is the interfacial energy between water and vapor, which is 72 mJ/m^2.

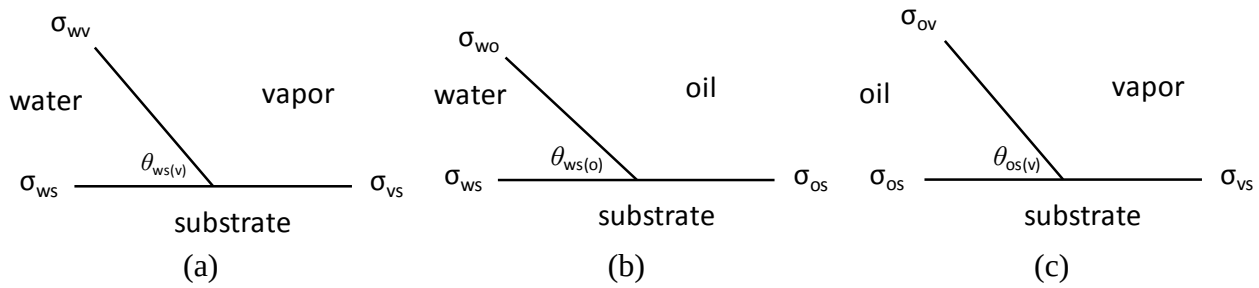

Figure F1. Schematics showing the relations between interfacial energies and contact angle using Young's equation for (a) water-vapor-substrate, (b) water-oil-substrate, and (c) oil-vapor-substrate systems.

Similarly, with the introduction of oil which surrounds the water droplet on a surface, the local contact angle, $\theta_{ws(o)}$, can be determined as

$$cos\theta_{ws(o)} = \frac{\sigma_{os} - \sigma_{ws}}{\sigma_{wo}} = \frac{\sigma_{os} - \sigma_{vs} + \sigma_{vs} - \sigma_{ws}}{\sigma_{wo}} \quad \text{(E14)}$$

where σ_{os} is the interfacial energy between the surface and oil, σ_{ws} is the interfacial energy between water and the surface, and σ_{wo} is the interfacial energy between water and oil, which is 49 mJ/m^2.[5]

Since σ_{os} is experimentally difficult to obtain for our system, we provide bounds for the local contact angle for the water-oil-substrate system, $\theta_{ws(o)}$, as follows. We consider the contact angle of oil on the high-surface-energy domain using

$$cos\theta_{os(v)} = \frac{\sigma_{vs} - \sigma_{os}}{\sigma_{ov}} \quad \text{(E15)}$$

where σ_{ov} is the interfacial energy between vapor and oil, which is 17 mJ/m^2. Since the oil wets the TFTS-coated surface, which means $\theta_{os(v)}$<90º. Therefore, we can determine that 0<$\sigma_{vs} - \sigma_{os}$<17 mJ/m^2.

As a result, the local contact angle of the water droplet on a surface surrounded by oil can be bounded as

$$cos\theta_{ws(o)} = \frac{\sigma_{os} - \sigma_{vs} + \sigma_{vs} - \sigma_{ws}}{\sigma_{wo}} \in \left(\frac{-17 + 36}{49}, \frac{0 + 36}{49}\right) \quad \text{(E16)}$$

$$\therefore \theta_{ws(o)} \in (43°, 67°)$$

S3. Derivation of nucleation rate as a function of contact angle and interfacial energy

The nucleation rate, *J*, can be determined by classical nucleation theory (CNT) as[6]

$$J = zf^* \exp(-G^*) \tag{E17}$$

In Eqn. (E13), *z* is the Zeldovich factor and *G** is the dimensionless energy barrier, given by

$$z = (kT \ln S)^2 / 8\pi v_o \sqrt{kT\psi(\theta)\gamma^3} \tag{E18}$$

$$G^* = 16\pi\psi(\theta) v_o^2 \gamma^3 / 3(kT)^2 (\ln S)^2 \tag{E19}$$

where *S* is the supersaturation and $\psi(\theta)$ is the activity that accounts for the effect of contact angle. *f** is the frequency of monomer attachment to the critical droplet nucleus dependent on the nature of the nucleus growth. The main modes of growth during heterogeneous nucleation are limited *via* direct impingement of monomers to the nucleus or surface diffusion [7-8].

The frequency of monomer attachment due to direct vapor impingement is given by

$$f^*_i = \gamma_n[(1 - \cos(\theta_w))/2\psi^{2/3}(\theta)](36\pi v_o^2)^{1/3} I n^{2/3} \tag{E20}$$

where γ_n is the sticking coefficient ($0 < \gamma_n < 1$), *I* is the classical Hertz-Knudsen impingement rate ($I = P/\sqrt{2\pi m_o kT}$), *n* is the number of molecules in the nucleated cluster, and v_o is the volume of an individual water molecule (v_o = 3 x 10^{-29} m^3). To determine an upper bound on the nucleation rate, a sticking coefficient of one was assumed (γ_n = 1).

The frequency of monomer attachment due to surface diffusion is given by

$$f^*_{\mathrm{sd}} = \gamma_{\mathrm{n}} c^* \lambda_{\mathrm{s}}{}^2 I \tag{E21}$$

where c^* is the capture number due to surface diffusion ($1 < c^* < 5$), and λ_s is the mean surface diffusion distance of an adsorbed monomer on the substrate. The capture number c^* is size independent and approximately equal to 1.9 for heterogeneous condensation of water vapor [9]. The mean surface diffusion distance is dependent on the wettability of the substrate and is given by $\lambda_{\mathrm{s}} = \sqrt{D_{\mathrm{sd}} \tau_{\mathrm{d}}}$ where D_{sd} is the surface diffusion coefficient ($D_{\mathrm{sd}} = d_{\mathrm{s}}{}^2 \nu_{\mathrm{s}} \exp[-E_{\mathrm{sd}}/kT]$), τ_{d} is the desorption time ($\tau_{\mathrm{d}} = (1/\nu_{\mathrm{s}}) \exp[-E_{\mathrm{des}}/kT]$), ν_{s} is the adsorbed molecule vibration frequency determined using the Debye approximation ($\nu_{\mathrm{s}} = V_D a/2$), d_{s} is the length of a molecular jump along the substrate surface approximated by the lattice constant of the substrate (d_{s} = 5.4 Å) [10] and V_{D} is the speed of sound in the substrate (V_{D} = 8433 m/s). The desorption and surface diffusion energies are given by $E_{\mathrm{des}} = E_1 + \sigma_{\mathrm{sv}} a_{\mathrm{o}}$ and $E_{\mathrm{sd}} = 0.5 E_{\mathrm{des}}$ [11], respectively, where E_1 is the binding energy of an n = 1 sized cluster, σ_{sv} is the solid-vapor interfacial energy and a_{o} is the water molecule surface area (a_{o} = 4.67 x 10^{-19} m^2). The calculated energies of desorption show excellent agreement with that of the experiments and molecular dynamics simulations ($E_{\mathrm{des,SiO2}}$ = 0.9 eV) [12-13].

By adding the nucleation rate from the two mechanisms together, the nucleation rate, J, can be determined as a function of the contact angle and interfacial energy of the condensate at given supersaturations, as shown in Fig. 2k in the paper.

S4. Control experiments on homogeneous hydrophobic surfaces

Dimethyldicholorosilane (DMCS), which is a homogeneous hydrophobic coating, was used in

our studies for control experiments. DMCS can be deposited on silicon surfaces using the vapor deposition process as described in the Methods section.

An atomic force microscope (AFM) image of a flat silicon surface coated by DMCS is shown in Fig. F2a. We did not observe any high-surface-energy domains with the coatings. The advancing and receding contact angles on the DMCS coated surface were measured to be θ_a/ θ_r = 103.8° ± 0.5°/102.7° ± 0.4°, respectively. The hysteresis was significantly lower compared to TFTS-coated surfaces, which also indicates the homogeneity of the DMCS coating.

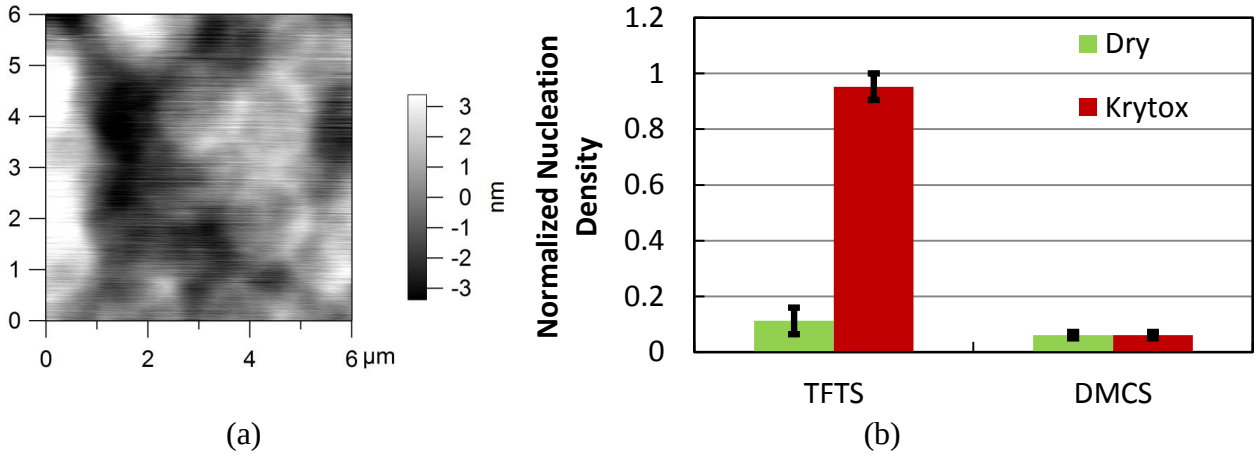

(a) (b)

Figure F2. (a) AFM height images of flat silicon surfaces coated with DMCS. The coatings are homogeneous. (b) Comparison of nucleation densities on surfaces with TFTS and DMCS coatings. The nucleation densities were normalized against pillar densities to obtain a fair comparison.

Condensation experiments were performed on micropillar arrays coated by DMCS with and without oil-infusion using the same experimental setup for the condensation experiment on TFTS-coated micropillar arrays, as described in the Methods section. The results are summarized and compared to the TFTS-coated surfaces in Fig. F2b. The nucleation density was normalized against the density of pillars for a fair comparison between different geometries. The nucleation density increase was not observed on DMCS-coated surfaces even after oil-infusion, as predicted by classical nucleation theory. Note that classical theory predicted nucleation rates as low as 0.2 $m^{-2}s^{-1}$ on TFTS-coated surfaces without oil-infusion. However, in our experiments, we

observed some rare nucleation as shown in Fig. F2b as well as in Supplemental Video V1. Repeated condensation experiments showed that nuclei formation and droplet pinning occurred on identical spots for each subsequent test, indicating that the spots are defects in the silane coatings where the hydrophilic silicon oxide surface (contact angle $\theta = 38^{o}$) was exposed. Such defects, while limited in number, act as nucleation sites for condensation.

S5. Heat transfer measurement apparatus and experimental procedure

A custom environmental chamber was built to test the heat transfer performance of each sample for the study. The vacuum chamber (Kurt J. Lesker) was made of stainless steel with two viewing windows. Resistive heater lines were wrapped around the exterior of the chamber walls to prevent condensation at the inside walls, and the chamber was wrapped with insulation on the exterior walls. Two insulated stainless steel water flow lines (Swagelok) were fed into the chamber *via* a KF flange port (Kurt J. Lesker) to supply cooling water to the chamber from a large capacity chiller (System III, Neslab). A flow meter (7 LPM MAX, Hedland) having an accuracy of ± 2% was integrated along the water inflow line.

A secondary stainless steel tube line was fed into the chamber *via* a KF adapter port that served as the flow line for the incoming water vapor supplied from a heated steel water reservoir. The vapor line was wrapped with a rope heater (60 W, Omega) and controlled by a power supply (Agilent). The vapor reservoir was wrapped with another independently-controlled rope heater (120 W, Omega) and insulated to limit heat losses to the environment. The access tubes were welded to the vapor reservoir, each with independently-controlled valves. The first valve

(Diaphragm Type, Swagelok), connecting the bottom of the reservoir to the ambient, was used to fill the reservoir with water. The second valve (BK-60, Swagelok), connecting the top of the reservoir to the inside of the chamber, was used to provide a path for vapor inflow. K-type thermocouples were located along the length of the water vapor reservoir to monitor temperature.

To obtain the temperatures within the chamber, K-type thermocouple bundles were connected through the chamber apertures *via* a thermocouple feed through (Kurt J. Lesker). A pressure transducer (925 Micro Pirani, MKS) was attached to monitor pressure within the chamber. The thermocouple bundles and the pressure transducer were both connected to an analog input source (RAQ DAQ, National Instruments), which was interfaced to a computer to record and store data. A second bellows valve (Kurt J. Lesker) on the chamber was connected to a vacuum pump to bring the chamber down to vacuum conditions prior to vapor filling. A liquid nitrogen cold trap was placed between the chamber and vacuum pump which served to remove any moisture from the pump-down process.

To run the test samples inside the chamber, the stainless steel bellows tube lines (1/4", Swagelok) were connected to the external water flow lines. T-connection adapters (Swagelok) with bore through Ultra-Torr fittings (Swagelok) were used to adapt K-type thermocouple probes (Omega) at the water inlet and outlet. Prior to experimentation, the thermocouple probes were calibrated using a high precision temperature controlled bath (Lauda Brinkman) to an accuracy of ± 0.2 K. The test samples, 6.35 mm diameter tubes with different surface treatments, were connected *via* a Swagelok compression fitting onto the T-connection. Chilled water flows through the inlet bellows tube, along the inside of the tube sample and through the outlet. Two supports were used to hold the sample and the entire configuration in place. Two separate pieces of insulation were embedded with K-type thermocouple leads and used for wet bulb temperature

measurements during experimental runs. A third thermocouple was placed beside the sample to measure the reference temperature inside the chamber. As the experiment progressed, the wet-bulb insulating wick collected water from the bottom of the chamber to the embedded thermocouple. The temperature measured by this thermocouple was compared to the reference temperature calculated from the saturation pressure. This allowed for a high accuracy secondary measurement of saturation conditions inside the chamber. Figure F3 shows the schematic of the test setup for the heat transfer performance measurement.

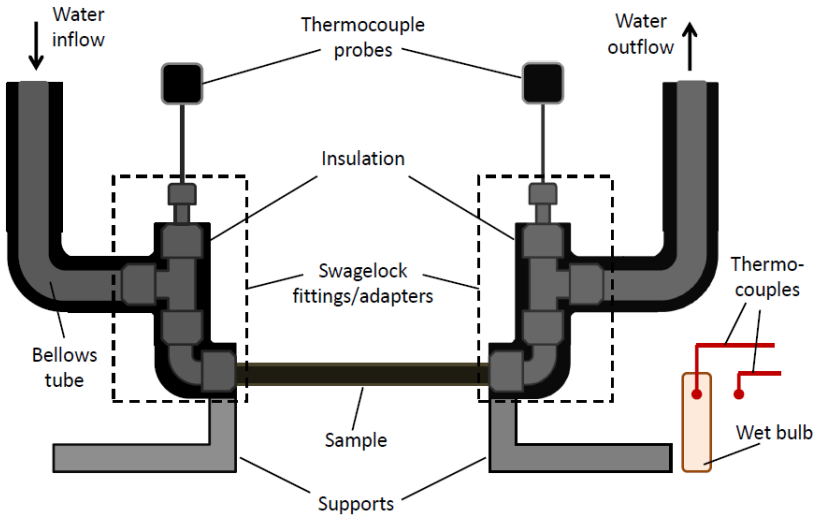

Figure F3. Schematic of experimental setup inside the chamber (not to scale). The heat flux was determined by the temperature rise in the water from inlet to outlet. The temperature difference was calculated as the log mean temperature difference (LMTD) between the chilled water and the vapor. The actual vapor pressure was found using the wet bulb temperature near the condensing surface.

For each experimental trial, a set of strict procedures were used to ensure consistency throughout the experiments. The water vapor reservoir was filled with approximately 3.5 liters of DI water (99% full) using a syringe through the vapor release valve. After opening the vapor inflow valve and closing the vapor release valve, the rope heater around the water vapor reservoir was turned on and the heater controller set to maximum output. Then the rope heater connected to the vapor inflow valve was turned on. The temperature of the water reservoir was monitored with the

installed thermocouples. Once boiling was achieved and all thermocouples on the reservoir reached > 95˚C for at least 10 minutes, the vapor inflow valve was closed.

The next step was to begin the vacuum pump-down procedure. Valves connecting the chamber with the ambient, and valves connecting the chamber and the vacuum pump were both closed while the valve connected to the liquid nitrogen cold trap was opened. The vacuum pump was then turned on, initiating the pump-down process where the pressure inside the chamber was carefully monitored. This process took ≈30 minutes in order to achieve the target non-condensable gases pressure (≈30 Pa).

After pumping down, the vapor inflow valve was opened to allow steam flow into the chamber and condensation occurred on the surface of the tube. The heat flux was determined by the rise in the temperature of the chilled water from the inlet to the outlet. The temperature difference, ΔT was determined as the log-mean temperature difference (LMTD) between the vapor and the chilled water.[14] Each data point in Fig. 4 of the manuscript was determined over 10 minutes of steady state operation. After that, the vapor inflow valve was adjusted to change the vapor pressure in the chamber. The error bars in Fig. 4 were determined based on the uncertainty in the thermocouple and flow rate measurement. The duration of each experimental run was around 45 – 60 minutes. The thermal conductivity of the Krytox GPL 100 oil was 0.08-0.09 W/mK.[15] The associated conduction thermal resistance of the oil layer is very small due to the small thickness (≈1 μm). The oil-infusion was found to be very stable over days without significant change in heat transfer performance.

S6. Droplet Shedding Radius

The experimentally-determined average droplet shedding radii ($\hat{R}$) for a typical dropwise hydrophobic surface (Figure F4a) and a Krytox oil-infused immersion condensation surface (Figure F4b) were determined *via* direct measurement through frame-by-frame analysis of high speed video. Videos (90 frames per second) of the condensation process taken at ≈2.4 kPa vapor pressure were analyzed to determine the radius of droplets that slide down from the top half of the surface and clean the surface for re-nucleation. Droplet size measurements were taken just prior to droplet sliding down the tube (to avoid coalescence effects). The shedding radius was averaged for 50 droplets for each tube sample and was determined to be $\hat{R}_{DHP}$ = 1.83 ± 0.31 mm and $\hat{R}_{IC}$ = 0.98 ± 0.13 mm on the typical dropwise hydrophobic and oil-infused surfaces, respectively. Reported error is due to droplet shedding variance from droplet to droplet.

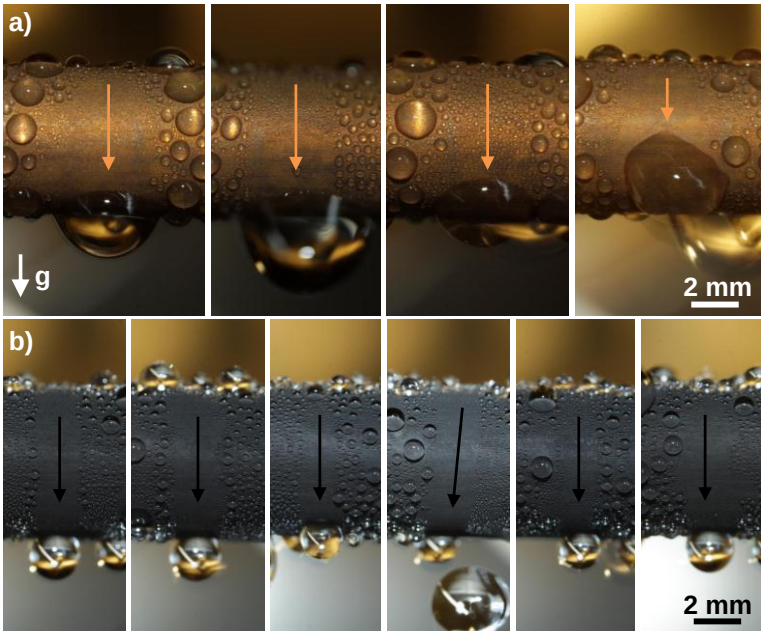

Figure F4. Droplet shedding radii on a (a) dropwise hydrophobic surface and a (b) Krytox oil-infused immersion condensation surface. The images show the tube samples immediately after a droplet shed down and clean the surface for re-nucleation. Orange and black arrows indicate direction of droplet motion during droplet shedding on DHP and IC surfaces, respectively.

S7. Supplemental Videos

All the videos were taken using a Phantom V7.1 high speed camera (Vision Research Inc).

V1. Condensation behavior on TFTS-coated silicon micropillar array. The pillar diameters are 5 μm and periods are 15 μm. The supersaturation in the experiment is $S = 1.6$. Almost no nucleation was observed except on sparse defects in the TFTS coating where hydrophilic silicon oxide substrate was exposed. The video was recorded with 10 frames per second (fps) and is played back at 30 fps.

V2. Immersion condensation behavior on oil-infused TFTS-coated silicon micropillar array. The pillar geometries and experimental conditions are the same with Video V1. Nucleation occurred on every tip of the pillars, which yields over an order of magnitude higher nucleation density compared to Video V1. The video was recorded with 10 fps and played back at 30 fps.

V3. Condensation on a regular hydrophobic copper tube. The tube is horizontally placed with chilled water flowing inside with flow rate of 5 L/min. The vapor pressure in the experiment is ≈2.4 kPa. Droplet grow and coalesce before removed by gravity at diameters around 2 mm. The video was recorded with 30 fps and played back at 30 fps.

V4. Condensation on an oil-infused TFTS-coated copper oxide tube. The tube is horizontally placed with chilled water flowing inside with flow rate of 5 L/min. The vapor pressure in the experiment is ≈2.4 kPa. Higher droplet density was observed compared to Video V3 while the departure diameter is reduced to approximately 0.98 ± 0.13 mm. The video was recorded with 30 fps and played back at 30 fps.

References

1. Miljkovic, N.; Enright, R.; Wang, E. N., Effect of Droplet Morphology on Growth Dynamics and Heat Transfer during Condensation on Superhydrophobic Nanostructured Surfaces. *Acs Nano* **2012,** *6* (2), 1776-1785.
2. Umur, A.; Griffith, P., Mechanism of Dropwise Condensation. *J Heat Transf* **1965,** *87* (2), 275-&.
3. Kim, S.; Kim, K. J., Dropwise Condensation Modeling Suitable for Superhydrophobic Surfaces. *J Heat Trans-T Asme* **2011,** *133* (8).
4. Rose, J. W., On the mechanism of dropwise condensation. *International Journal of Heat and Mass Transfer* **1967,** *10* (6), 755-762.
5. Anand, S.; Paxson, A. T.; Dhiman, R.; Smith, J. D.; Varanasi, K. K., Enhanced Condensation on Lubricant Impregnated Nanotextured Surfaces. *Acs Nano* **2012**.
6. Kashchiev., D., *Nucleation: Basic Theory with Applications*. 1 ed.; Oxford: Butterworth-Heinemann.: 2000.
7. Pound, G. M.; Simnad, M. T.; Yang, L., Heterogeneous Nucleation of Crystals from Vapor. *The Journal of Chemical Physics* **1954,** *22* (7), 1215-1219.
8. Sigsbee, R. A., Adatom Capture and Growth Rates of Nuclei. *J Appl Phys* **1971,** *42* (10), 3904-3915.
9. Pocker, D. J.; Hruska, S. J., Detailed Calculations of the Number of Distinct Sites Visited in Random Walk on Several Two-Dimensional Substrate Lattices. *Journal of Vacuum Science and Technology* **1971,** *8* (6), 700-707.
10. J.P.Hirth; G.M.Pound, *Condensation and evaporation - nucleation and growth kinetics* England: Pergamon Press.: 1963.
11. Thiel, P. A.; Madey, T. E., The interaction of water with solid surfaces: Fundamental aspects. *Surface Science Reports* **1987,** *7* (6–8), 211-385.
12. Israelachvili, J. N., *Intermolecular and surface forces*. 2nd ed.; Academic Press: Amsterdam, 1991.
13. Ma, Y.; Foster, A. S.; Nieminen, R. M., Reactions and clustering of water with silica surface. *The Journal of Chemical Physics* **2005,** *122* (14), 144709-9.
14. Mills, A. F., *Heat and Mass Transfer*. 2 ed.; Prentice-Hall: 1999.
15. Dupont http://www2.dupont.com/Lubricants/en_US/assets/downloads/H-58505-4_Krytox_Overview_LowRes.pdf.